Indian Journal of Pure & Applied Physics
Vol. 64, March 2026, pp. 316-326
DOI: 10.56042/ijpap.v64i3.26459

Synthesis of ZnO–TiO₂ Hybrid Nanoparticles via Plasma Jet Technique for Enhanced Photocatalytic and Antibacterial Applications

Tamara A Hameed[a], Al-Behadili Faisal Raheem[b], Ali Q Tuama[c] &
Rajaa Obayes Abdulsada[d*]

[a]Department of GeoPhysics, College of Remote Sensing and Geophysics, Al Karkh University of Science, Baghdad, Iraq
[b]Department of Medical Physics, College of Applied Medical Sciences, University of Kerbala, Karbala, Iraq
[c]Department of Physics, Al-Kharkh University of Science, College of Science, Baghdad, Iraq
[d]Department of Medical Physics, Al Taff University College, Karbala, Iraq

Received: 11th December 2025; accepted: 12th January 2026

ZnO, TiO_2, and ZnO–TiO_2 hybrid nanostructures were synthesized using an atmospheric-pressure plasma jet as a fast and solvent-free approach. Optical emission spectroscopy confirmed the formation of a stable oxygen plasma with an electron temperature of approximately 0.83 eV and an electron density of $\sim 1.7 \times 10^{17}$ cm^{-3}. XRD analysis revealed well-defined crystalline phases with average crystallite sizes of about 12 nm for ZnO, 16 nm for TiO_2, and 14 nm for the ZnO–TiO_2 hybrid. Optical studies showed a significant band gap reduction to 2.68 eV for the hybrid compared with the individual oxides. The ZnO–TiO_2 hybrid exhibited superior photocatalytic activity toward methylene blue degradation under natural sunlight, achieving a degradation efficiency of 94.26% with a pseudo-first-order rate constant of 0.036 min^{-1}. Antibacterial evaluation demonstrated enhanced inhibition zone diameters of 29 mm against Staphylococcus aureus and 25 mm against Escherichia coli. The improved performance is attributed to efficient interfacial charge separation and enhanced reactive oxygen species generation at the ZnO–TiO_2 heterojunction.

Keywords: ZnO, TiO_2, ZnO/TiO_2, Photocatalytic, Plasma jet

1 Introduction

Nano substances are one of the most significant and promising new categories of materials and are highly demanded in a broad variety of applications in practice[1,2]. The distance in between five silicon atoms, or ten hydrogen atoms aligned in a row, is one nanometer[3,4]. Nanomaterials are a new, discrete category of materials, with chemical and physical properties not similar to those of larger materials, and with sizes ranging between one nanometer and one hundred nanometers[5,6]. The significant enhancement in several properties is reached to an enhancement in the surface to volume ratio at the nanoscale[7,8]. Recent developments in nanotechnology have led to the ability of researchers to make a range of these materials with specificity[9,10]. Nanomaterials can also be formed using downward methods where atoms or molecules are brought together into nanoparticles[11,12]. Downward processes, in contrast, are physical mechanisms, which include milling, lithography, and intensive evaporation to make larger materials in the range of nanoscale to be used in many industries[13]. Metal oxides can be produced in a number of methods, some of them being thermal, liquid-phase, and physical milling[14,15]. The synthesis of nanomaterials through alternative, cheap, and environmentally friendly processes is of great concern to most researchers[16,17]. A more recent development is the suggestion of a quick, inexpensive synthetic method of making metal oxides through plasma[18,19]. Although the temperatures of low-temperature, non-equilibrium plasma are low, it has many benefits when developing metal oxide nanostructures of a specific size and shape even at room temperature[20]. The devices based on plasma also have a number of advantages, such as less energy usage, simplicity of installation, affordable price, air-pressure discharge, and possible use in various industrial sectors. Some of the types of plasma sources are dielectric barrier discharge (DBD), corona discharge, micro-discharge, and flame systems[21-24]. Among other properties are their unparalleled characteristics over other substances that make metal oxides very important in many medical, industrial, and technological applications[25,26]. Metal oxides, which

---

*Corresponding author: E-mail: rajaaabdulsada776@gmail.com

include zinc oxide, copper oxide among others are very good materials in optical and photonic applications as they are used in light absorption, photo-transmission, and photo-sensing, among others[27]. This is because they have low energy gap, thus making the transfer of energy to be smoother and efficient to transfer electrons, particularly in photocatalysis making its performance much better than other materials[28].

Several studies have investigated plasma-assisted fabrication of ZnO–TiO$_2$ composite systems using different plasma configurations. For example, one study investigated the synthesis of heterogeneous TiO$_2$/ZnO composite molecules by treating mixed oxide powders with low-temperature atmospheric plasma, where plasma was mainly employed to promote surface activation and interfacial contact between the two phases, leading to improved photocatalytic degradation of organic dyes[29]. In another study, dielectric barrier discharge (DBD) plasma was applied as a post-synthesis surface modification technique to enhance defect density and charge separation in oxide-based semiconductor composites, resulting in improved photocatalytic efficiency compared with untreated samples[30]. Although these plasma-assisted approaches demonstrated performance enhancement, plasma was not utilized as the primary synthesis route for direct oxide formation and controlled hybridization, which remains a key limitation in previously reported works.

In contrast to conventional chemical routes and previously reported plasma-based techniques, the present study introduces an atmospheric-pressure plasma jet as a solvent-minimized, vacuum-free, and low-temperature strategy for the direct synthesis of ZnO–TiO$_2$ hybrid nanostructures. Unlike sol–gel or hydrothermal methods that rely on chemical precursors, long reaction times, and post-annealing treatments, the plasma jet enables in situ oxidation and heterojunction formation through energetic electron–gas interactions under ambient conditions. A key novelty of this work lies in integrating plasma diagnostics via optical emission spectroscopy (OES) to quantitatively correlate electron temperature and density with nanoparticle formation, crystallite size reduction, and interfacial charge-transfer behavior. Furthermore, the sequential plasma exposure approach facilitates controlled ZnO–TiO$_2$ hybridization without secondary phases, leading to enhanced charge separation, suppressed recombination, and superior photocatalytic and antibacterial performance. These features collectively distinguish the atmospheric-pressure plasma jet technique as a scalable and chemically clean alternative for engineering multifunctional oxide heterostructures.

2 Materials and Methods

2.1 Materials

A 6 cm × 2 cm × 1 mm thick piece of 99.99% pure zinc and a 99.99% pure titanium piece of the exact dimensions were purchased from Sigma-Aldrich. PVP powder was also obtained from the same company, and these materials were prepared to begin the plasma jet nanomaterial synthesis process.

2.2 Plasma Jet System Description and Experimental Conditions

The plasma jetting system was made to run at atmospheric pressure and was comprised of high voltage power of up to 17 kV and a cutoff frequency of 100 kHz. It also incorporated a gauge of the rate of flow of gas to regulate the process as it goes on with this rate being set at 3 liters per minute. Oxygen gas was purified and was introduced through tubing to a plasma nozzle needle that was a cylinder of 2 mm diameter made of stainless steel. The tip of the needle was connected to the negative electrode and the other electrode was attached to the target metal object[31]. The sampling between the electrodes was kept at around 2 cm to guarantee the maximum performance. The metal target was put in a glass flask that had 10 mL of deionized water. The flask was placed 2 cm away to the plasma nozzle which would provide even distribution of energy in the preparation. The first preparation of zinc nanoparticles involved placing a piece of zinc in the solution and subjecting the solution to the plasma system after 10 minutes which produced zinc oxide nanoparticles. The same steps were followed in preparing titanium oxide nanoparticles. In the case of the hybrid compound, the preparation of zinc particles was done in the same conditions. After that the particle of zinc was substituted with a titanium particle in the same solution with zinc oxide, which led to the creation of the hybrid compound, ZnO- TiO 2. All samples were subjected to the same conditions of the experiment to obtain similar results and be reproducible. Figure 1 depicts how the plasma diagnostics system was set up in the experiment to make nanomaterials[32].

During all experiments, the plasma jet was operated under stable discharge conditions with continuous operation mode, fixed electrode spacing, and constant gas flow rate. Each sample was exposed to the plasma for the same treatment duration to ensure reproducibility of the synthesis process.

3 Results and Discussion

3.1 Optical Diagnosis of Oxygen Plasma via OES

Figure 2 (a) shows the optical emission spectrum of the oxygen plasma. The resulting plasma emits distinct spectral lines, with a maximum emission at the O2 wavelength of 390.7 nm, indicating a high electron density. Other O2 or O3 lines appear within the range of 314–783 nm, reflecting varying degrees of excitation and ionization within the plasma. This confirms the stability of the resulting plasma and its ability to emit characteristic spectral lines. The selected oxygen spectral lines used for electron temperature and density calculations were chosen based on their strong intensity, clear separation, and reliable spectroscopic parameters reported in the NIST database. These lines are commonly employed in atmospheric-pressure plasma diagnostics to ensure accurate and reproducible determination of plasma parameters.

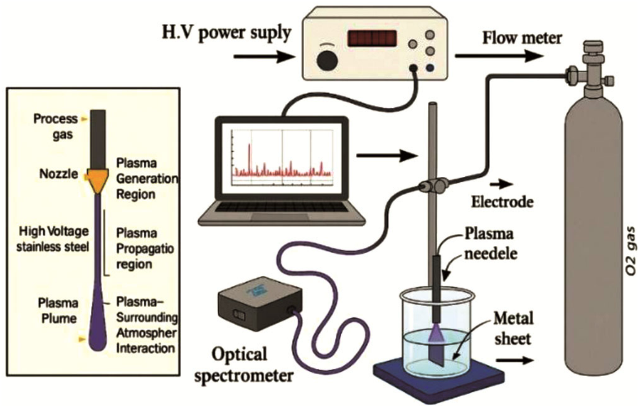

Fig. 1 — Schematic steps for sample preparation using plasma jet technique

Figure 2 (b) shows a magnified image at 390 nm, used to calculate the plasma electron density according to Strak's analysis. The results show an electron density of approximately 1.7 × 10^{17} cm^{-3}, indicating that the plasma undergoes continuous collisions, thus maintaining the distinct O2 lines. The electron density was calculated using the equation below[33].

$$n_e\,(\mathrm{cm}^{-3}) = \left(\frac{\Delta\lambda_{\mathrm{FWHM}}}{2w}\right) \times 10^{17} \qquad \ldots (1)$$

This equation represents the dependence of the electron density ne on the Full Width at Half Maximum (FWHM), where Δλ FWHM denotes the spectral line width at half its maximum intensity, and w denotes the line width at its minimum intensity[34].

Figure 2 (c) shows the Boltzmann diagram used to calculate the electron temperature. Five spectral lines from the emitted spectrum were used and compared with the National Institute of Standards and Technology (NIST) database. By plotting the relationship between the energy of the highest energy level (Ej) and the logarithm of the spectral line intensity ln $(\lambda_{ji} I_{ji}/A_{ji} g_j)$ A negatively sloped line is obtained. The equation below was used to calculate the electron temperature in the plasma.

$$\ln\left[\frac{\lambda_{ji} I_{ji}}{hcA_{ji} g_j}\right] = \frac{1}{k_B T}\left(E_j\right) + \ln N/U(T) \qquad \ldots (2)$$

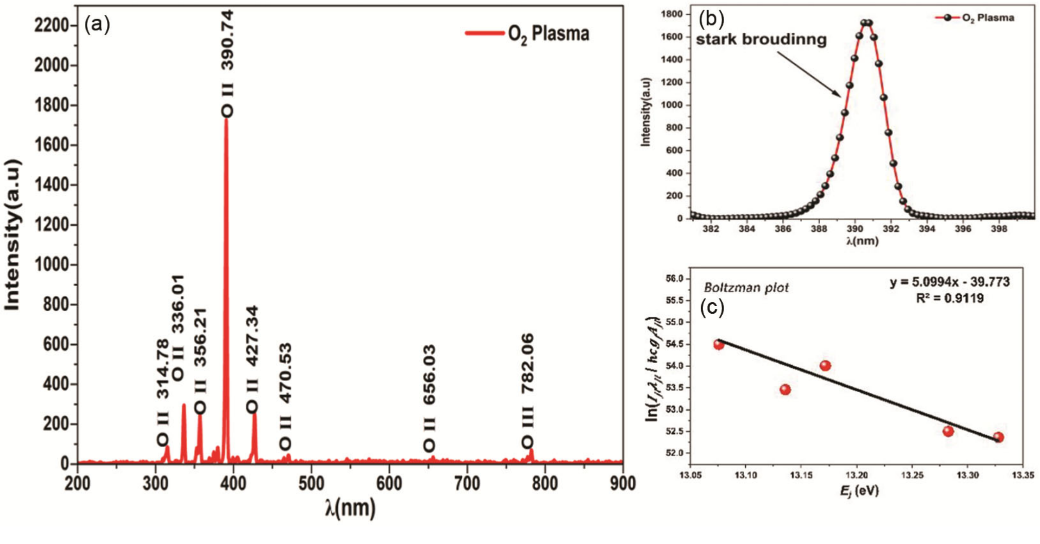

Fig. 2 — (a) The emitted oxygen plasma spectrum, (b) The stark broadening used to calculate electron density, and (c) The Boltzmann Plot used to calculate electron temperature

Equation (2) shows the dependence of ln ($\lambda_{ji}I_{ji}/A_{ji}g_j$) versus Ej, where λ_{ji}Represents the radiation intensity at wavelength λ; Ej is the maximum energy associated with this wavelength; h is Planck's constant; c is the speed of light in a vacuum; kB is the Boltzmann constant[35].

From this slope, the electron temperature was determined to be approximately 0.83 eV. This value matches to the atmospheric pressure plasma which is both a cold plasma and at the same time contains enough electrons that are hot enough to ionize oxygen atoms. All in all, these values reveal the stability of the plasma and the capability to generate nanomaterials to be used in the processes like the extraction of organic pollutants in water including methylene blue[36].

The measured electron temperature and density play a key role in controlling oxidation kinetics and nucleation processes, thereby influencing nanoparticle formation and crystallite size during plasma jet synthesis.

The stability of the plasma parameters was monitored throughout the synthesis duration under fixed operating conditions (constant applied voltage, gas flow rate, and electrode spacing). Repeated OES measurements recorded at different time intervals during plasma exposure showed no noticeable shift in the main oxygen emission lines or significant variation in Stark broadening profiles. Accordingly, both electron density and electron temperature remained within a narrow fluctuation range, indicating a stable plasma discharge during the entire nanoparticle synthesis process.

3.2 XRD analysis

The X-ray spectrum of ZnO, TiO_2 and ZnO/TiO_2 hybrid is represented in Fig. 3. The findings show that when the crystals of both materials are prepared in the plasma, the crystal structure does not change but does not form any unwanted secondary phase. ZnO lines present at angles (100), (002), (101), (102), (110), and (112), are attributed to the hexagonal structure of zinc oxide whereas the TiO_2 lines present at angles (101), (004), (200), (105), and (211) are attributed to the anatase phase of titanium oxide[28]. The spectrum of the ZnO/TiO_2 composite reveals the overlapping of the characteristic lines of the two phases which proves the creation of hybrid crystal structure which allows the charge-carrier flow interface (heterojunction) and increases the separation of the electrons and holes which is indispensable to the increase of the optical efficiency. A comparative analysis of the main diffraction peaks confirms that all samples retain their characteristic crystal structures, with noticeable peak broadening in the hybrid sample. This broadening reflects reduced crystallite size and increased interfacial strain induced by the plasma-assisted hybridization process.

The width of the peptide at half-maximum (FWHM) was analyzed and using the Scherrer equation, the crystal size of ZnO was determined to be 12 nm whereas the crystal size of TiO_2 was determined to be around 16 nm. The hybrid composite experienced a moderate reduction to 14 nm in crystal size which is a necessary measure that the plasma preparation reduces crystal growth and makes them identifiable in a discrete nanoscale range. Overall, these findings suggest that the obtained materials have both a consistent crystalline structure and a small nanoscale size and can be used in high-efficiency photocatalytic and biochemical applications[37].

3.3 FESEM and EDX Characterization

Figure 4 shows the morphological and elemental compositional study of ZnO, TiO_2 and the ZnO/TiO_2 hybrid nanoparticles synthesized with the use of plasma jetting. FESEM images of the ZnO sample demonstrate that the product nanoparticles are rather homogeneous, possess a quasi-spherical structure, and are assembled in few aggregates, with average diameter of about 22 nm, which indicates the creation of stable crystals in vacuum conditions. Conversely, the TiO_2 images show a more scattered, fragmented structure with an average size of 18 nm, which is

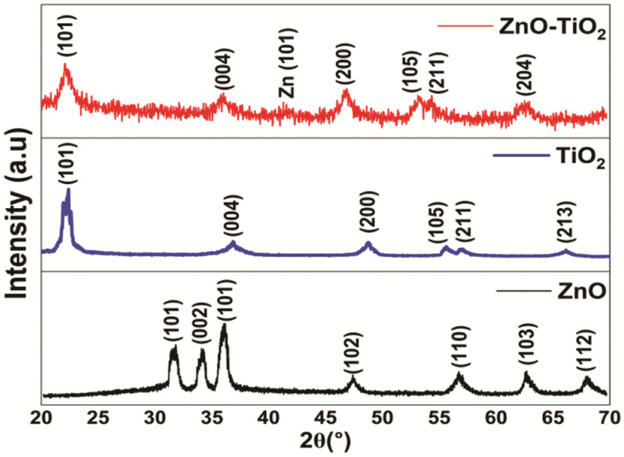

Fig. 3 — XRD pattern of ZnO, TiO_2 and the ZnO–TiO_2 hybrid compound

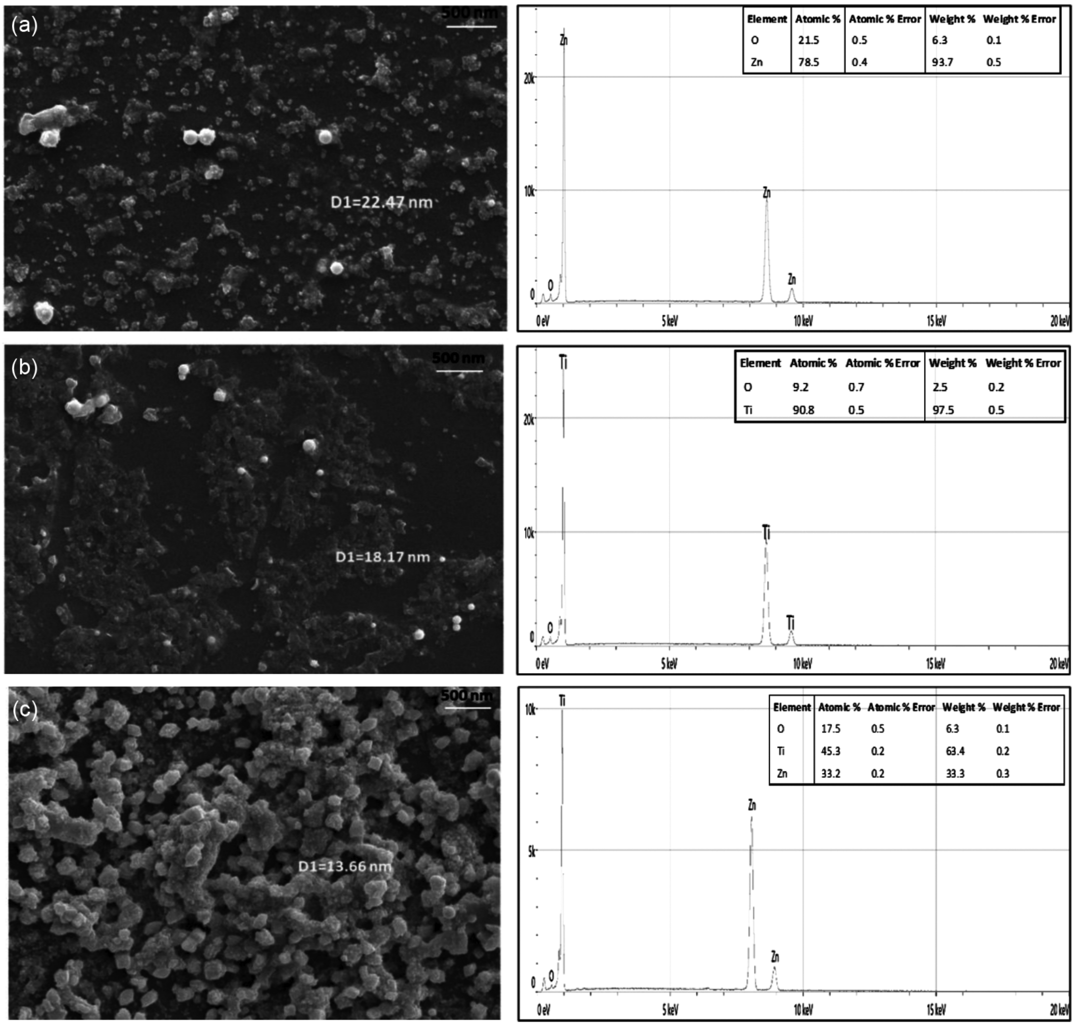

Element	Atomic %	Atomic % Error	Weight %	Weight % Error
O	21.5	0.5	6.3	0.1
Zn	78.5	0.4	93.7	0.5

Element	Atomic %	Atomic % Error	Weight %	Weight % Error
O	9.2	0.7	2.5	0.2
Ti	90.8	0.5	97.5	0.5

Element	Atomic %	Atomic % Error	Weight %	Weight % Error
O	17.5	0.5	6.3	0.1
Ti	45.3	0.2	63.4	0.2
Zn	33.2	0.2	33.3	0.3

Fig. 4 — FESEM and Edx images of samples prepared by plasma jet method (a) ZnO, (b) TiO2, and (c) ZnO-TiO2

anatase phase, which is highly vulnerable to the development of microparticles in the influence of plasma[38]. Lastly, FESEM images of the ZnO/TiO_2 hybrid also show a higher-order and more closely bonded structure with a much smaller nano size of 13 nm. It is believed to be due to the interface reactions between the two oxides that inhibit growth favoring formation of more coherent hybrid crystalline structure. The reported particle sizes were estimated by averaging measurements from multiple representative regions in the FESEM images. The hybrid sample exhibits reduced agglomeration and more uniform particle distribution compared with the individual oxides, indicating improved structural integration at the nanoscale.

The EDX spectra (in the real figure) prove the purity of the prepared samples. According to the structure of the materials, the sample of ZnO contains only zinc and oxygen, whereas the sample of TiO_2 has a regular distribution of titanium and oxygen. In addition, the outcomes of ZnO/TiO_2 hybrid compound illustrate the existence of all three components, Zn, Ti and O in the proportional amounts. Overall results of morphological and elemental analysis of the nanoparticles prepared in the plasma jetting demonstrates the efficiency of the procedure adopted in the manufacture of nanoparticles in the targeted and miniature manner. The EDX spectra reveal the presence of the elements of Zn, Ti, and O with stable elemental ratios in the analyzed areas, and it proves the successful formation of the $ZnO-TiO_2$ hybrid structure. The impurity-related peaks were not observed, which presupposes great compositional purity of the made samples. This has made it a feasible alternative in light-based applications like photocatalytic applications and other environmental applications.

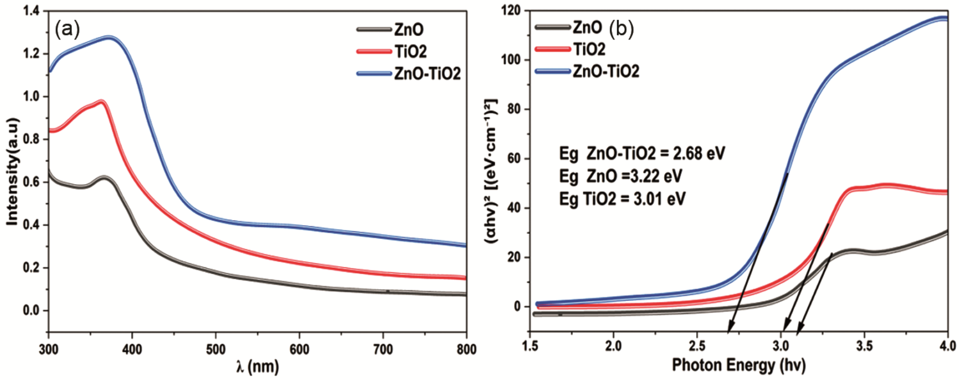

Fig. 5 — Absorption spectra and Tauc curves for ZnO, TiO_2 and ZnO–TiO_2 samples

Table 1 — Elemental composition of ZnO, TiO_2, and ZnO–TiO_2 samples obtained from EDX analysis

Sample	Zn (at.%)	Ti (at.%)	O (at.%)
ZnO	48.6	–	51.4
TiO_2	–	33.2	66.8
ZnO–TiO_2	21.5	18.7	59.8

The elemental composition of the prepared samples was further analyzed using EDX, and the corresponding atomic percentages are summarized in Table 1.

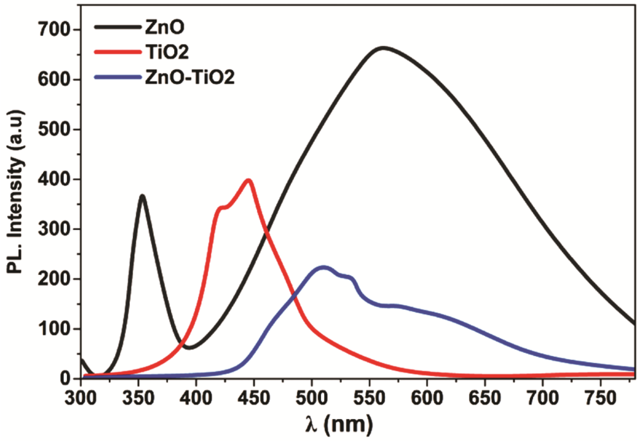

Fig. 6 — Photoluminescence (PL) spectra of ZnO, TiO_2 and ZnO–TiO_2 samples, showing the difference in emission intensity and the change in peak positions due to the difference in defect centers and the effect of the hybrid structure

3.4 Optical Characterization

Figure 5 demonstrates the optical characteristics of the ZnO, TiO 2, and ZnO/ TiO 2 hybrid samples in the 300-800 nm region. An absorption edge in the sample of ZnO was detected at approximately 370 nm and this indicated a lower band gap. The absorption edge of TiO_2 sample changed to a shorter value of 390 nm, which is typical of anatase phase with an energy gap of approximately 3.0 eV. In case of the ZnO/TiO_2 hybrid, the findings revealed that the oxide had an absorption edge, but the energy was at a higher value thus the beam structure had changed due to development of a hybrid interface between the two oxides.

A Tauc plot also supported this behavior and gave band-gap values of the prepared samples. ZnO had a band gap of 3.22 eV and TiO_2 3.01 eV, which is in line with some of the literature results[39]. Nonetheless, the reduction in the band gap of the ZnO/TiO_2 hybrid compound became pronounced to 2.68 eV. This reduction means that there is an electronic communication between the two oxides and the creation of new energy pathways at the interface. These channels reduce the distance between the conduction and the valence bands (VB and CB) and, therefore, increase absorption of the hybrid compound in the visible range and its optical efficiency. The diminished band gap traits confirm that the hybrid construction does not just maintain the characteristics of the two oxides but might also give constructive carrier separation system that reduces recombination. This gives the resulting product more efficient in photocatalytic reaction[40].

Similar band gap reduction behavior has been reported for ZnO–TiO_2 heterojunction systems, where interfacial electronic coupling and enhanced charge-transfer processes were identified as the dominant factors governing the optical response and visible-light absorption[41]. The reduction in the band gap of the ZnO–TiO_2 hybrid is primarily associated with interfacial electronic coupling and charge-transfer transitions at the ZnO/TiO_2 heterojunction. While defect states may contribute to band tailing, the dominant role of interface states is supported by the strong suppression of PL intensity, indicating efficient charge separation rather than defect-driven recombination.

In Fig. 6, the Photoluminescence (PL) spectrum of ZnO, TiO_2 and the ZnO/TiO_2 hybrid nanomaterials are presented. The findings indicate different optical behaviours with respect to a variation in electronic structure and the character of the defect centres in each material. In the sample of ZnO, the presence of a strong and broad pulse of light in the range of 350-700 nm indicates the presence of many centers of defects on the surface and oxygen deficiency. This enhances the likelihood of electron-hole recombination which results in an increased PL emission. Conversely, the TiO_2 sample has a narrow peak at PL at about 430- 470 nm corresponding to anatase phase that has fewer defect centers and is more ordered in structure thereby lowering the intensity of emission[42].

Lastly, in the case of ZnO/TiO_2 hybrid compound, a large reduction in the PL intensity and expansion between 450-600 nm was observed in the spectrum. This observation may be explained as an evidence of improved carrier separation among the two oxides and low recombination probability because of the creation of a hybrid interface that can conduct electron transfer between the two elements. This low PL of the compound signifies increased photocatalytic efficiency because the emission is weaker and thus it implies a lower rate of recombination, thus enhancing the electron-hole lifetime hence better the activity of the catalyst in terms of activation under illumination[43].

The pronounced suppression of PL intensity in the $ZnO–TiO_2$ hybrid indicates a significant reduction in radiative electron–hole recombination due to efficient charge separation at the heterojunction interface. This prolonged carrier lifetime enhances the availability of reactive charge carriers at the catalyst surface, which directly explains the superior photocatalytic degradation efficiency and higher reaction kinetics observed for the hybrid sample under sunlight irradiation.

The formation of a true $ZnO–TiO_2$ heterojunction rather than a simple physical mixture is supported by the combined structural and optical evidence. The noticeable bandgap narrowing, and the significant suppression of PL intensity indicate interfacial charge transfer and efficient carrier separation, which cannot be achieved by physical mixing alone. Additionally, the reduced crystallite size observed in the hybrid XRD pattern suggests interfacial interaction between ZnO and TiO_2 phases.

3.5 Photocatalytic Activity

The prepared nanoparticles were tested in terms of photocatalytic activities in order to assess their ability to degrade organic dyes. Methylene Blue (MB) was used. The solution of dye was taken at the concentration of 10 mg/L and nano liquids of ZnO, TiO_2 and ZnO/TiO_2 were introduced ZnO, TiO_2, and ZnO/TiO_2. The solution was allowed to remain in the dark with a magnetic stirrer to ensure that there was a balance between adsorption and absorption. The solution was finally subjected to nature sunlight between 10:00AM and 2:00 PM. The absorption of samples taken after every 30 minutes of drift of the dye solution which contained the nanoparticles was determined at the level of characteristic wavelength of the methylene blue (l = 664). All the three samples were subjected under the same conditions to guarantee proper, consistent outcomes and reproducibility of the experiments[36].

Figure 7 indicates the reduction in spectral absorption intensity of the methylene blue dye at the wavelength of 664 nm with time in the presence of sunlight at the prepared nanoparticles. A gradual decrease in the intensity of absorption was noticed in the case of ZnO, which is a good indication of moderate photocatalytic activity because it forms electron-hole pairs. The reduction in the intensity of absorption was comparatively more rapid in the case of TiO_2 because the activation phase is more efficient because of highly active anatase phase.

In the case of ZnO/TiO_2 hybrid compound, the extinction rate was the greatest at the MB peak over a period of time, which means that the catalytic performance of photocatalyst was greatly enhanced. This may be explained by the fact that a hybrid interface between the two oxides is formed to enable the separation of the electrons and holes and hence, the reduction of recombination. It results in the increased lifetime of the active charge carriers, which directly accelerates the dissociation of the methylene dye molecules.

Figure 8 shows how the C/C0 ratio of the methylene blue dye changes after exposing the dye to the sun rays in the presence of the prepared nanoparticles. The relative concentration of ZnO is reduced comparatively in the case whereas TiO_2 shows a much better performance. Also, the ZnO/TiO_2 hybrid material has the greatest concentration decrease throughout the exposure period, which shows a high photocatalytic performance by the synergistic effect at the two oxide interfaces.

The logarithmic curve (C/C_0) shows a clear linear correspondence for the three materials, confirming that the photocatalytic decomposition process follows

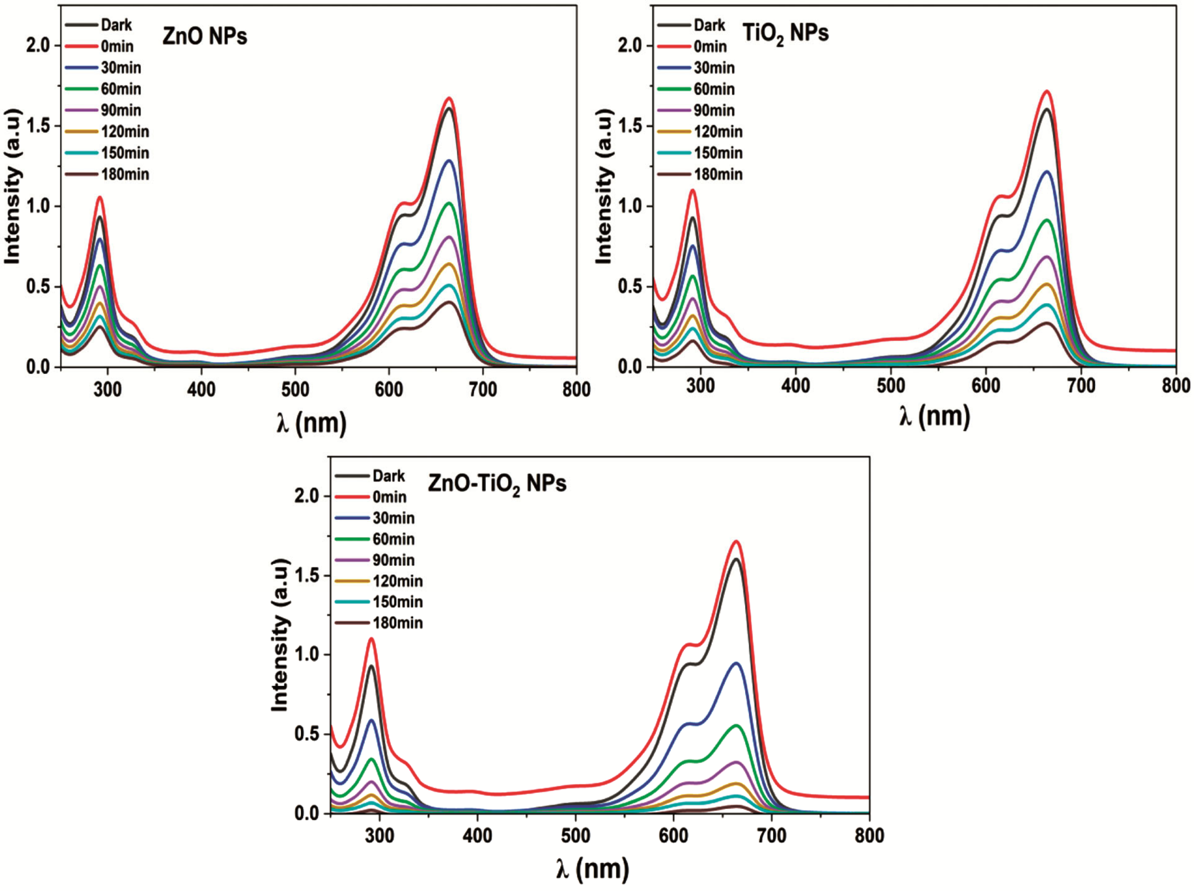

Fig. 7 — Absorption of methylene blue dye in the presence of ZnO, TiO_2, and ZnO–TiO_2 nanoparticles during exposure to sunlight

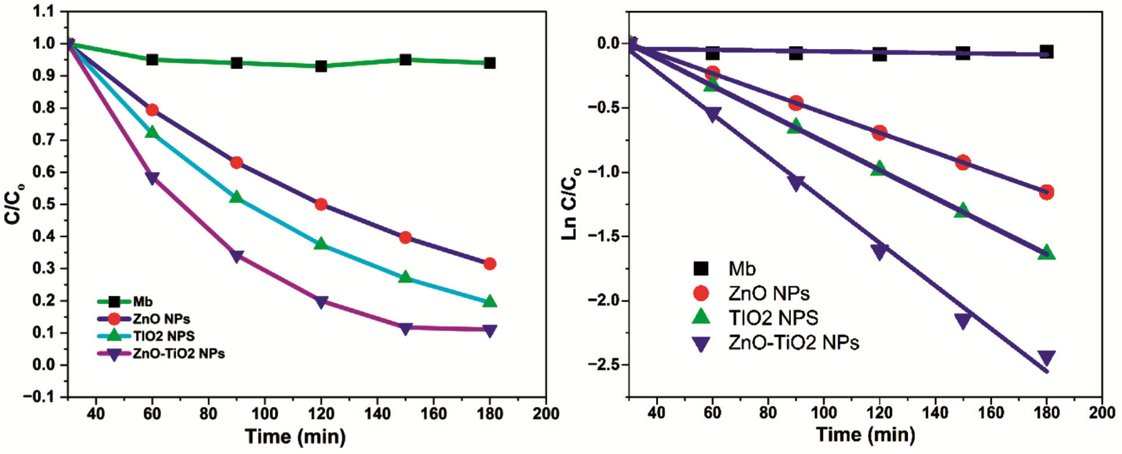

Fig. 8 — Concentration change curves of methylene blue dye (C/C_0) and $\ln(C/C_0)$ curves in the presence of nanocatalysts under sunlight

pseudo-first-order kinetics. The velocity constant K was calculated using the equation of motion[44].

$$\ln\left(\frac{C}{C_0}\right) = -K_{ap}\, t \qquad \dots (3)$$

K_{ap} represents the apparent rate constant for a pseudo-first-order reaction, where Co (in mol/L) refers to the initial dye concentration, and C (mol/L) represents the dye concentration at time t (in min).

The degradation efficiency was calculated using the equation[45].

$$Degradation\ efficincy = \frac{(C_0 - C)}{C_0} * 100\% \dots .(4)$$

C stands for the dye concentration at a presumptive reaction time, and Co for the dye's initial concentration.

The obtained results show that the decolorization efficiency reached 82.54%, 88.47%, and 94.26% for ZnO, TiO_2, and the ZnO–TiO_2 hybrid nanocomposite, respectively, indicating a cooperative interfacial effect that enhances charge carrier utilization and suppresses recombination. Similarly, the apparent rate constants (k) were determined to be 0.028 min^{-1}, 0.033 min^{-1}, and 0.036 min^{-1}, respectively, with the hybrid sample exhibiting the highest kinetic value. The pseudo-first-order kinetic plots showed good linearity with regression coefficients (R^2) exceeding 0.98 for all samples, confirming the reliability of the kinetic fitting. Overall, these results demonstrate that the formation of a ZnO–TiO_2 hybrid interface significantly improves charge separation, prolongs electron–hole lifetime, and leads to enhanced photocatalytic degradation rates and decolorization efficiency compared with the individual oxides[46].

3.6 Antibacterial Activity

Against Staphylococcus aureus and Escherichia coli, the antibacterial activity of the plasma-synthesized nanomaterials- ZnO, TiO_2 and the hybrid ZnO-TiO_2 was evaluated against them by using agar-well diffusion method. Nutrient agar was ready and poured into Petri dishes and sterilized. All the bacterial strains were incubated in nutrient broth at 37 degC, 18- 24 h, and the turbidity of the suspension was adjusted to the 0.5 McFarland standard (approximately 108 CFU/mL). The uniform bacterial lawn was prepared by placing the inoculum on the agar surface. In each plate (A, B, C and D) 4 wells (6 mm) were prepared: A (control: DI water), B (ZnO nanoparticles), C (TiO_2 nanoparticles), and D (ZnO-TiO_2 nanocomposites). Each sample was placed in 50 microliters in its given well and the plates incubated at 37 degC over 24 h. The inhibition zones were measured thrice, and the results became mean +- SD.

Figure 9 depicts antibacterial reaction of the nanomaterials tested. Control (A) always gave low

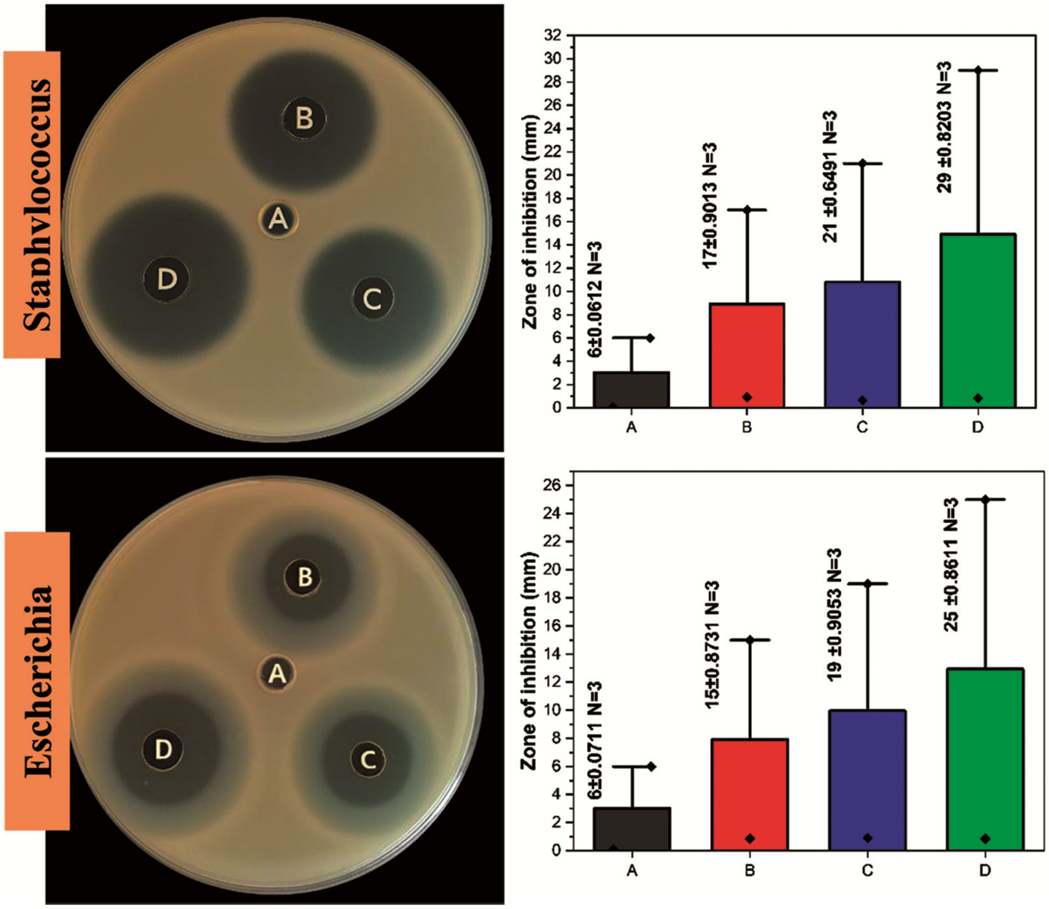

Fig. 9 — Antibacterial activity of samples A–D against Staphylococcus aureus and Escherichia coli showing inhibition zones on agar plates and corresponding zone-diameter values

activity (~6 mm) with both bacterial strains, and this agreed that the source of inhibition is entirely due to the nanomaterials. The sample of ZnO (B) had a moderate inhibition ability on both S. aureus (17 mm) and E. coli (15 mm) because ZnO could produce reactive oxygen species (ROS) and partially interacts with the bacterial membrane. The TiO_2 sample (C) exhibited better antibacterial activities with a maximum of between 21 mm and 19 mm against S. aureus and E. coli respectively, due to a higher reactivity of the surface and the production of ROS at ambient conditions based on defects. Hybrid nanocomposite (D) of ZnO-TiO_2 was the most active with an activity of 29 mm and 25 mm on S. aureus and E. coli, respectively. This dramatic increase is explained by the heterojunction type of structure that is created between ZnO and TiO_2, and enhances the electron-hole distance, enhances the ROS generation, and boosts the oxidative assault on the cell walls. Membrane rupture, cytoplasmic leakage, and inhibition of metabolic pathways are also made possible by the synergistic effect to enable the hybrid nanocomposite to overcome Gram-positive and Gram-negative bacterial defenses[47].

The higher antibacterial activity observed against Staphylococcus aureus compared to Escherichia coli is mainly related to differences in cell wall structure. As a Gram-positive bacterium, S. aureus lacks an outer lipopolysaccharide membrane, allowing easier nanoparticle interaction and ROS penetration. In contrast, the additional outer membrane in Gram-negative E. coli acts as a diffusion barrier, partially limiting nanoparticle attachment and oxidative damage[48].

The ZnO-TiO_2 hybrid nanocomposite has an antibacterial effect which occurs in a multi-stage mechanism, which is depicted in Fig. 10. When combined with the bacterial surface, the nanoparticles bind with a great affinity to the cell membrane because of its high surface energy and electrostatic interaction. The first contact aids penetration of the hybrid nanocomposite through the bacterial cell, which produces direct membrane disruption and intracellular components leakage[49].

After internalization the ZnO-TiO_2 heterojunction promotes the separation of electrons and holes; thus, resulting in the efficient production of reactive oxygen species (ROS) including hydroxyl radicals (OH) superoxide anions (O2 -), and hydrogen peroxide (H2O2). These ROS attack vital cellular targets leading to oxidative damages on DNA, proteins and ribosomal structures. Simultaneously, ROS damage the electron transport chain further contributing to the impairment of cellular respiration and metabolic activity. The result of membrane rupture, oxidative stress, enzymatic inactivation and genetic damage builds up to overwhelm the bacterial defense system and cause irreversible cell death[50].

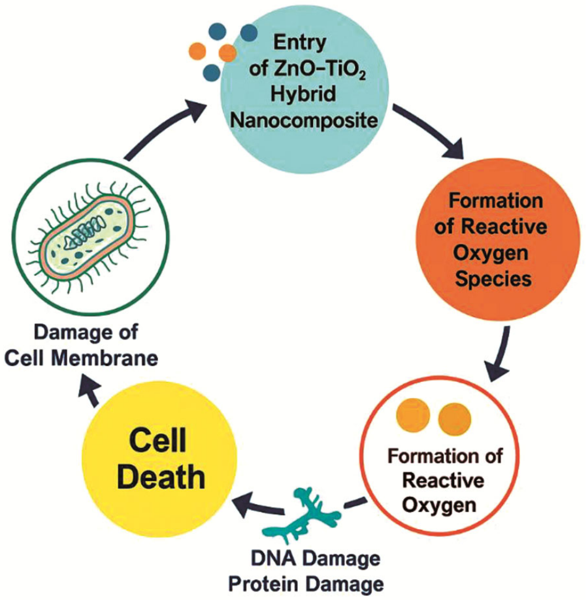

Fig. 10 — Proposed antibacterial mechanism of the ZnO–TiO_2 hybrid nanocomposite, illustrating nanoparticle entry, membrane disruption, ROS generation, damage to cellular components (DNA and proteins), and the subsequent progression toward bacterial cell death

4 Conclusion

Atmospheric-pressure plasma jet synthesis successfully produced ZnO, TiO_2, and ZnO–TiO_2 hybrid nanostructures under stable plasma conditions, with an electron temperature of ~0.83 eV and an electron density of ~1.7×10^{17} cm^{-3}. XRD analysis revealed average crystallite sizes of approximately 12 nm for ZnO, 16 nm for TiO_2, and 14 nm for the ZnO–TiO_2 hybrid, while optical studies showed a pronounced band gap reduction to 2.68 eV for the hybrid compared with 3.22 eV (ZnO) and 3.01 eV (TiO_2), indicating effective heterojunction formation. The ZnO–TiO_2 hybrid exhibited superior photocatalytic activity toward methylene blue degradation under natural sunlight, achieving a degradation efficiency of 94.26 % with a pseudo-first-order rate constant of 0.036 min^{-1}. In addition, enhanced antibacterial performance was observed for the hybrid, with inhibition zone diameters of 29 mm against Staphylococcus aureus and 25 mm against Escherichia coli, confirming its multifunctional photocatalytic and antimicrobial capability.

References

1 Seo H J, Yu J H, Ananth A, Jeong R H & Boo J H, *Catalysts*, 12 (2022) 1020.

2 Rashid T M, Rahmah M I, Mahmood W K, *et al.*, *Plasmonics*, 20 (2025) 8461.

3 Sonpir R, Dake D, Raskar N, *et al.*, *Environ Sci Pollut Res*, 32 (2025) 1308.

4 Duraisamy M, Sreekantan S, Govindasamy G A *et al.*, *J Sol-Gel Sci Technol*, 115 (2025) 1156.

5 Jawad M H & Abdulameer M R, *Iraqi J Sci*, 64 (2023) 1210.

6 Suliman Z A, Mecha A C & Mwasiagi J I, *Discov Chem*, 2 (2025) 32.

7 Sonpir R B, Dake D V, Raskar N D, *et al.*, *Ceram Int*, 50 (2024) 28746.

8 He J, Yang Z, He W, *et al.*, *J Mater Sci*, 60 (2025) 15245.

9 Jawad M H & Abdulameer M R, *AIP Conf Proc*, 2922 (2024) 150003.

10 Li X F, Ding Y, Wang J, *et al.*, *Water Air Soil Pollut*, 236 (2025) 7.

11 Mane V, Dake D, Raskar N, *et al.*, *Chem Phys Impact*, 8 (2024) 100517.

12 Mane V A, Dake D V, Raskar N D, *et al.*, *Results Chem*, 6 (2023) 101083.

13 Sonpir R B, Dake D V, Raskar N D, *et al.*, *Chem Select*, 10 (2025) e04702.

14 Jawad M H, Assi A A & Hameed A M, *Plasmonics*, 20 (2025) 7883.

15 Sonpir R B, Dake D V, Raskar N D, *et al.*, *Mater Today Commun*, 38 (2024) 108076.

16 Mane V A, Dake D V, Raskar N D & Dole B N, *Mater Sci Future Appl*, (2025) 287.

17 Sarabyar S, Farahbakhsh A, Tahmasebi H, A *et al.*, *Reac Kinet Mech Cat*, 138 (2025) 2407.

18 Fahem M Q, Jawad M H, Abdulsada R O, *et al.*, *Ionics*, 31 (2025) 6475.

19 Shoman N, Solomonova E & Akimov A, *Environ Sci Pollut Res*, 32 (2025) 21450.

20 Saffari M, Ghorbanloo M, Morsali A, *et al.*, *Catal Lett*, 155 (2025) 132.

21 Jawad M H & Abdulameer M, *Eurasian Phys Tech J*, 22 (2025) 75.

22 Abdullah H A R, Fahem M Q, Turki Z T, *et al.*, *Eur Phys J E*, 48 (2025) 40.

23 Ummadi R R, Ratnakaram V N, Devineni S R, *et al.*, *Res Chem Intermed*, 51 (2025) 3767.

24 Nayak N, Singha S, Maity J P, *et al.*, *J Mater Sci Mater Electron*, 35 (2024) 310.

25 Fahem M Q, Mohsion H N, Turki Z T, Abdullah H A R & Jawad M H, *J Ovonic Res*, 21 (2025) 419.

26 Saleem M, Naz M Y, Shukrullah S, Ali S & Hamdani S T A, *Appl Phys A*, 127 (2021) 608.

27 Hassan A, Anwar S, Rashid R, *et al.*, *J Fluoresc*, 35 (2025) 7293.

28 Turki Z T, Fahem M Q, Mankhi Z A, *et al.*, *Russ Phys J*, 68 (2025) 804.

29 Noori N A & Aadim K A, *Iraqi J Appl Phys*, 21 (2025) 191.

30 Ali I H, Kadhim R T, Alasady D F A, *et al.*, *Theor Exp Chem*, 61 (2025) 148.

31 Khosravi S, Chaibakhsh N, Jafari S & Nilkar M, *Sci Rep*, 14 (2024) 28385.

32 Jawad M H & Abdulameer M R, *Ind J Phys*, 99 (2025) 4845.

33 Jawad M H & Abdulameer M R, *Russ Phys J*, 68 (2025) 903.

34 Jamal R K, Ali F H, Hameed M M & Aadim K A, *Iraqi J Sci*, (2020) 1032.

35 Hashim A J, Jaafar H M M, Mohsion H N, *et al.*, *Bio Nano Sci*, 15 (2025) 514.

36 Imran H J, Hubeatir K A & Aadim K A, *Sci Rep*, 13 (2023) 5441.

37 Jawad M H, Abdulameer M R & Aadim K A, *Sci Tech J Inf Technol Mech Opt*, 25 (2025) 626.

38 Abdaalameer N K, Mazhir S N & Aadim K A, *Chalcogenide Lett*, 18 (2021) 405.

39 Khosravi S, Chaibakhsh N, Jafari S & Nilkar M, *Sci Rep*, 14 (2024) 28385.

40 Kassymov A, Adylkanova A, Bektemissov A, *et al.*, *Int J Thermophys*, 47 (2026) 2.

41 Zhang Y, Bo X, Zhu T, *et al.*, *Nanomater*, 14 (2024) 1802.

42 Hussain W D, Jawad M H, Khaleel S F, *et al.*, *Russ Phys J*, 68 (2025) 1750.

43 Buchtelik S, Chrastny V, Sochacki A, *et al.*, *Discov Water*, 4 (2024) 126.

44 Bouiri E, Omari L H, Dahbi S, *et al.*, *Euro-Mediterr J Environ Integr*, 10 (2025) 1595.

45 Hussein A S, Jawad M H, Abdulsada R O, *et al.*, *J Mater Sci Mater Electron*, 36 (2025) 2036.

46 Hussein A S, Dulaimi S, Al-Asady B A J, *et al.*, *J Mater Sci Mater Electron*, 36 (2025) 2080.

47 Athab Z H, Halbus A F, Mohammed S B, *et al.*, *Sci Rep*, 14 (2024) 4032.

48 Hussain Z A, Fakhri F H, Alesary H F & Ahmed L M, *J Phys Conf Ser*, 1664 (2020) 012064.

49 Ismail H K, Alesary H F, Juma J A, *et al.*, *Electrochim Acta*, 418 (2022) 140348.

50 Alesary H F, Ismail H K, Kareem J H, *et al.*, *Surf Coat Technol*, 475 (2023) 130160.

51 Odda A H, Cheang T Y, Alesary H F, *et al.*, *J Mater Chem B*, 10 (2022) 1453.